This is the peer reviewed version of the following article: [Sensitivities of slantwise convection dynamics to model grid spacing under an idealized framework. Quarterly Journal of the Royal Meteorological Society 147, 736 p1930-1948 (2021)], which has been published at https://doi.org/10.1002/qj.4003

Sensitivities of slantwise convection dynamics to model grid spacing under an idealized framework

Ting-Chen Chen*, Man-Kong Yau, Daniel J. Kirshbaum

Department of Atmospheric and Oceanic Sciences, McGill University, Montreal, Quebec, Canada

*corresponding author email: ting-chen.chen@mail.mcgill.ca

Keywords: slantwise convection, conditional symmetric instability, numerical weather prediction, grid spacing sensitivity

Funding information: NSERC/Hydro-Quebec Industrial Research Chair program and the Fonds de recherché du Québec – Nature et technologies (FRQNT) (doctoral research scholarship grant).

Abstract

Although the release of conditional symmetric instability (CSI) by slantwise convection is recognized as an important baroclinic process, the basic dynamics of these circulations and their representation in numerical models remain inadequately understood. To address this issue, a series of 2D idealized experiments of pure slantwise convection are performed in an initially statically stable environment using the non-hydrostatic Weather Research and Forecasting Model, with the horizontal grid lengths varying between 1 to 40 km. The results show that the larger-scale feedbacks of the slantwise convection converge numerically when a cross-band grid length (Δy) of 5 km is reached. The differences between the non-converged and converged results tie closely to the release of a shallow layer of conditional instability that inevitably accompanies the early development of the slantwise circulation due to differential advection of saturation equivalent potential temperature (θ_e^*). The resolved small-scale upright convection embedded within the slantwise band can energize the horizontal acceleration of the slantwise band at mid-to-upper levels by transporting low geostrophic momentum upward that results in localized inertial instability. The convective cell also enhances the large-scale CSI neutralization by advecting high θ_e^* downward with strong downdrafts that orient more vertically than coarser-gridded runs. Moreover, $\Delta y \leq 5$km also better resolves the horizontal pressure gradients for cross-band motions. This work suggests that global/climate numerical weather prediction models may not adequately resolve important characteristics of slantwise convection. As most cumulus schemes target only upright convection, the inclusion of parameterized slantwise convection may improve their performance.

1. Introduction

The importance of moist symmetric instability in the atmosphere, in particular conditional symmetric instability (CSI), has been extensively studied since the pioneering work of Bennetts and Hoskins (1979), who proposed it to be one of the mechanisms for frontal rainbands in baroclinic environments. Since then, numerous observational studies have provided evidence of slantwise convection, the process by which CSI is released, often in the form of single or multiple quasi-linear bands (e.g., Bennetts and Sharp 1982, Emanuel 1988, Reuter and Yau 1990, 1993). Moreover, moist symmetric neutrality (but conditional stability) is often observed in the trailing precipitation regions of squall lines (e.g., Zhang and Cho 1992, Jiang and Raymond 1995) and in the ascent regions within cyclones (e.g., Emanuel 1988). Emanuel (1988) suggested that such findings indicate that slantwise convective adjustment occurs continuously on a smaller time scale than larger-scale baroclinic processes (e.g., frontogenesis) that generate CSI. In addition to its direct impact on precipitation, slantwise convection may drive the formation of sting jets (e.g., Gray et al. 2011, Baker et al. 2014, Schultz and Browning 2017) and enhance moist frontogenesis to spin up cyclones in the midlatitudes (e.g., Kuo et al. 1991, Balasubramanian and Yau 1994a, b, 1995).

Despite numerous theoretical (e.g., Ooyama 1966, Hoskins 1974, Emanuel 1983a), numerical (e.g., Innocentini and Caetano 1992 (hereafter IC92), Thorpe and Rotunno 1989, Persson and Warner 1991, 1993, 1995 (hereafter PW91, PW93, PW95, respectively), Seman 1994) and observational (e.g., Reuter and Yau 1990, 1993, Thorpe and Clough 1991, Browning et al. 2001) studies on symmetric instability, only recently have the climatological aspects of CSI and its association with midlatitude weather systems been explored using global reanalysis data (e.g., Ma 2000, Glinton et al. 2017, Chen et al. 2018). Chen et al. (2018) examined all the Northern Hemisphere cyclones over the period 1979-2008 and found that the chance of slantwise convection occurrence increases with the coincident intensification rate of the cyclones. Furthermore, larger slantwise convective available potential energy (SCAPE or slantwise CAPE) but smaller CAPE are found for explosive cyclones than for non-explosive cyclones. Whereas SCAPE drops significantly during explosive intensification, it does not change notably over the lifetime of non-explosive cyclones. This result provides supporting (albeit indirect) evidence that slantwise convection may contribute to rapid cyclone intensification, as hypothesized by Kuo et al. (1991), Reuter and Yau (1993), and Balasubramanian and Yau (1994a, b, 1995).

Given its potential importance on the midlatitude climate, one may ask whether slantwise convection can be reasonably resolved in global climate models (or general circulation models; GCMs) and what resolution is required to capture its important features and larger-scale feedbacks? A typical slantwise convective band has a time scale of a few hours and a width of tens to hundreds of kilometers in the cross-band direction (e.g., Reuter and Yau 1990, Schultz and Schumacher 1999). Nonetheless, smaller-scale embedded processes might meaningfully affect its evolution. Most GCMs have horizontal grid lengths of O(10-100 km), for which parametrization of upright convection is needed. However, most cumulus parameterization schemes do not consider slantwise convection. While the impacts of horizontal grid spacing on simulated frontal bands in cyclones (e.g., Lean and Clark 2003) or squall lines (e.g., Bélair and Mailhot 2001) have been addressed, few studies have examined the grid-resolution sensitivity of pure slantwise convection. Thus, the resolution at which slantwise convection can be adequately (explicitly) resolved, and how significantly the failure to do so would impact the large-scale environment, remains unclear.

PW93 is one of a few studies to investigate the effects of model grid spacing on the unforced/free (with no external forcings applied) slantwise convective band in an environment that is stable to upright convection. They performed idealized simulations with a hydrostatic and viscous 2D version of the MM4 mesoscale model (developed by the Pennsylvania State University-National Center for Atmospheric Research) with horizontal grid spacings (Δy) ranging from 6 to 40 km. Their results show that the model simulates a slower and weaker development of slantwise convection with increasing Δy, but this sensitivity is less noticeable for $\Delta y \leq 15$ km. They thus concluded that one should strongly consider parameterization for slantwise convection for a horizontal grid spacing larger than 15 km, and possibly for even finer resolution in environments where the symmetric instability is weak. To understand such a grid-spacing sensitivity, PW93 solved the linear growth rate as a function of the updraft width (Xu 1986) and found that when the updraft width of the most unstable mode cannot be reasonably resolved in the model (i.e., the width is smaller than about 4 grid-lengths), a less unstable mode might be triggered. This results in a weaker growth rate of slantwise convection than that simulated at a finer grid spacing. Another study is Knight and Hobbs's (1988) numerical simulation of frontal development in an Eady wave, in which they reached a similar conclusion that hydrostatic slantwise convections were poorly resolved at a horizontal grid spacing of 40 km but reasonably resolved at a horizontal grid spacing of 10 km.

The purpose of this paper is to extend the work of PW93 on the sensitivity of pure and unforced slantwise convection to horizontal grid spacing to a non-hydrostatic framework, with the finest grid spacing reduced to 1 km to resolve smaller-scale and non-hydrostatic processes that could potentially affect band development. Another justification for revisiting the CSI problem is that many numerical studies in the 1980s and 1990s, including PW93 and IC92, intended to investigate CSI but actually examined potential symmetric instability (PSI) instead. This was a common misnomer pointed out by Schultz and Schumacher (1999). PSI is assessed using wet-bulb or equivalent potential temperature (θ_e) and such instability is *created* only if a potentially unstable layer first undergoes a finite vertical displacement to reach saturation. On the other hand, CSI is assessed with saturation equivalent potential temperature and the instability is called "conditional" because it exists locally only if the condition of saturation is met. The distributions of PSI and CSI may be substantially different, and they are equivalent only if the flow is saturated everywhere (Bennetts and Hoskins 1979, Schultz and Schumacher 1999).

The dynamics of slantwise convection are analyzed here using an inline momentum budget retrieval tool that accurately captures the tendencies associated with different forcing terms during the model integration (Chen et al. 2020). These analyses aid investigation of the main dynamical processes that are responsible for the grid-spacing sensitivity. We then examine how such sensitivities in momentum fields affect other thermodynamic fields and the associated larger-scale feedbacks. The organization of the paper is as follows. In Section 2, the basic principles and assessment of CSI are introduced. The governing equations, configuration, and setup of the numerical model are presented in Section 3. Section 4 presents the model results, including investigation of the dynamics governing the evolution of slantwise circulation and their sensitivities to the horizontal grid spacing. In Section 5, we provide some additional sensitivity tests. Finally, Section 6 presents the conclusions.

2. Identification of CSI and slantwise convection

The basic principles of symmetric instability are discussed in Emanuel (1994), Schultz and Schumacher (1999) and Markowski and Richardson (2010). The term "symmetric" refers to the 2D nature of this conceptual instability, assuming no variation along the thermal wind direction. Conceptually, symmetric instability is a mixture of static and inertial instabilities. Notably, although Ooyama's (1966) theoretical necessary and sufficient condition for symmetric instability[1] does not exclude static and inertial instabilities, "pure" symmetric instability is often considered to occur within

---

[1] The determinant or the trace (or possibly both) of the stability tensor in a meridional plane is negative. The stability tensor is defined as $\mathfrak{m} = \begin{pmatrix} F^2 & B \\ B & N^2 \end{pmatrix}$, where F^2 and N^2 are inertial stability and static stability, respectively, and B is the measure of baroclinicity.

environments that are both statically and inertially stable (e.g., Emanuel 1983a, b, Dixon et al. 2002, Chen et al. 2018). Pure symmetric instability involves both vertical and horizontal driving forces, resulting in a tilting structure with height toward the cool side of the baroclinic zone.

In a dry atmosphere, the environment is considered statically stable to infinitesimal upward movements if $\frac{\partial\bar{\theta}}{\partial z} > 0$, where θ is the potential temperature and the overbar indicates the hydrostatically balanced component. Defining the y axis as 90-degree counterclockwise to the geostrophic wind $\boldsymbol{V}_{\mathrm{g}}$, the environment is considered inertially stable to infinitesimal horizontal displacements in y if $\frac{\partial M_{\mathrm{g}}}{\partial y} < 0$, where

$$M_{\mathrm{g}} = u_{\mathrm{g}} - fy$$

is the geostrophic absolute/pseudo-angular momentum, u_{g} is the geostrophic (“zonal”; here along the x axis) wind and f is the Coriolis parameter. Pure dry symmetric instability exists in the above environment if $\bar{\theta}$ surfaces slope more steeply in the vertical than M_{g} surfaces in the y-z cross-section. A slantwise displacement of the air tube (of infinite extent in x) at an angle between the slopes of these two surfaces would result in positive accelerations in both horizontal (along y) and vertical directions.

The concept of symmetric instability can be extended to a moist atmosphere by replacing θ with the saturation equivalent potential temperature θ_{e}^{*}. The resulting dynamical instability is termed conditional symmetric instability (CSI). CSI can be viewed as conditional instability along an M_{g} surface, i.e., $\left.\frac{\partial\overline{\theta_{\mathrm{e}}^{*}}}{\partial z}\right|_{M_{\mathrm{g}}} < 0$, which is mathematically equivalent to negative saturation equivalent geostrophic potential vorticity in the Northern Hemisphere (e.g., Chen et al. 2018):

$$fMPV_{\mathrm{g}}^{*} < 0, \qquad \text{where} \quad MPV_{\mathrm{g}}^{*} = \frac{1}{\rho}\left[\nabla \times \boldsymbol{V}_{\mathbf{g}} + f\hat{\boldsymbol{z}}\right] \cdot \nabla\overline{\theta_{\mathrm{e}}^{*}}, \tag{1}$$

where ρ is the air density. Note that (1) does not guarantee pure CSI as both pure conditional and inertial instabilities can each contribute to negative MPV_{g}^{*}.

Another measure of the degree of CSI is the SCAPE, which has proven useful for studying developing frontal bands and cyclones (e.g., Shutts 1990, Gray and Thorpe 2001, Glinton et al. 2017). Sherwood (2000) argued that SCAPE is more appropriate for establishing a meaningful slantwise instability than the lapse-rate criterion ($\frac{\partial \overline{\theta_{\mathrm{e}}^{*}}}{\partial z}\Big|_{M_{\mathrm{g}}} < 0$). SCAPE is calculated analogously to CAPE but by lifting a hypothetical air tube (rather than parcel) along a slanted M_{g} surface instead of vertically (Emanuel 1983b):

$$\mathrm{SCAPE} = \int_{\mathrm{LFSC}}^{\mathrm{LSNB}}{}_{M_{\mathrm{g}}} R_{\mathrm{d}}(T_{\mathrm{vt}} - T_{\mathrm{ve}})\,d(-\ln p) \tag{2}$$

where T_{vt} and T_{ve} are the virtual temperatures of the lifted air and the environment, respectively, p is the pressure, and R_{d} is the gas constant for dry air. Here we confine the integral to the layer over which positive buoyancy is attained by the air tube. LFSC stands for the level of free slantwise convection and LSNB is the level of slantwise neutral buoyancy. SCAPE represents the maximum amount of potential energy available for conversion to kinetic energy and is not proportional to MPV_{g}^{*}. It should be noted that, as in upright convection where positive buoyancy can extend above the conditionally unstable layer, the buoyancy can remain positive above the negative MPV_{g}^{*} layer until the LSNB is reached (e.g., Stull 1991). Therefore, one should not downplay the role of CSI merely because the convective band extends into a positive MPV_{g}^{*} region (e.g., Zhang and Cho 1992). Many CSI studies approximated $\overline{\theta_{\mathrm{e}}^{*}}$ with θ_{e}^{*} and M_{g} with M (e.g., Shutts 1990, Emanuel 1988, Gray and Thorp 2001). While the former is generally valid, the latter can introduce large error when significant ageostrophy is present (Schultz and Schumacher 1999). Thus, in the current study, we use θ_{e}^{*} and M_{g} to assess CSI.

3. Methodology

3.1 Model and numerical setup

The numerical model used in this study is the compressible, non-hydrostatic, and idealized version of the Advanced Research Weather Research and Forecasting (WRF) model, version 3.8.1 (Skamarock et al., 2008). The model is run in 2D, with a domain size of 1600 km and 16 km in the *y* and *z* directions, respectively. The lateral boundaries are open in *y* and the lower boundary is free slip. The only subgrid parameterization scheme in use is the Thompson microphysics scheme (Thompson et al. 2008). Implicit Rayleigh damping for vertical velocity is activated over the uppermost 4 km of the domain to absorb vertically propagating internal gravity waves (Klemp et al. 2008). Six simulations with different horizontal grid spacings (Δy) of 40, 20, 10, 5, 2, and 1 km are conducted. The simulations are all carried out with a total of 130 vertical layers (stretched with an averaged vertical grid spacing of around 125 m; see more discussion in Section 5.1). Although no subgrid turbulence scheme is used for simplicity, the selected third- and fifth-order vertical and horizontal advection, respectively, contain implicit diffusion (Wicker and Skamarock 2002, Skamarock et al. 2008).

3.2 Governing equations and the inline budget retrieval

The WRF governing equations are formulated in flux form (Skamarock et al 2008). The momentum components, coupled with the dry air mass in the column, μ_d, are defined as

$$U = \mu_\mathrm{d} u, \qquad V = \mu_\mathrm{d} v, \qquad W = \mu_\mathrm{d} w, \qquad \Omega = \mu_\mathrm{d} \frac{d\eta}{dt},$$

where $\eta = \left(p_\mathrm{dh} - p_\mathrm{dh\_top}\right)/\mu_\mathrm{d}$ is the terrain-following vertical coordinate, in which p_dh stands for the hydrostatic pressure and $p_\mathrm{dh\_top}$ is the p_dh at the top of the dry atmosphere, *u*, *v*, and *w* are the velocity components parallel to the Cartesian *x*, *y*, and *z* axes, respectively, and $\frac{d\eta}{dt}$ is the vertical velocity on the η-coordinate. For our idealized setup on an f-plane, where $f = 1 \times 10^{-4}$ s^{-1}, these equations are written as

$$\underbrace{\frac{\partial U}{\partial t}}_{u\ \text{tendency}} = \underbrace{-\nabla \cdot (\boldsymbol{V}u)}_{\substack{\text{advection}\\ \text{ADV}_u}} \underbrace{-\mu_\mathrm{d}\alpha\frac{\partial p}{\partial x} - \frac{\alpha}{\alpha_\mathrm{d}}\frac{\partial p}{\partial \eta}\frac{\partial \phi}{\partial x}}_{\substack{\text{horizontal pressure gradient force}\\ \text{PGF}_u}} \underbrace{+fV}_{\substack{\text{Coriolis}\\ \text{COR}_u}} \underbrace{-\left(\frac{uW}{r_\mathrm{e}}\right)}_{\substack{\text{curvature}\\ \text{CUV}_u}} \tag{3}$$

$$\underbrace{\frac{\partial V}{\partial t}}_{v\ \text{tendency}} = \underbrace{-\nabla \cdot (\boldsymbol{V}v)}_{\substack{\text{advection}\\ \text{ADV}_v}} \underbrace{-\mu_\mathrm{d}\alpha\frac{\partial p}{\partial y} - \frac{\alpha}{\alpha_\mathrm{d}}\frac{\partial p}{\partial \eta}\frac{\partial \phi}{\partial y}}_{\substack{\text{horizontal pressure gradient force}\\ \text{PGF}_v}} \underbrace{-fU}_{\substack{\text{Coriolis}\\ \text{COR}_v}} \underbrace{-\left(\frac{vW}{r_\mathrm{e}}\right)}_{\substack{\text{curvature}\\ \text{CUV}_v}} \tag{4}$$

$$\underbrace{\frac{\partial W}{\partial t}}_{w\ \text{tendency}} = \underbrace{-\nabla \cdot (\boldsymbol{V}w)}_{\substack{\text{advection}\\ \text{ADV}_w}} + \underbrace{g\left(\frac{\alpha}{\alpha_\mathrm{d}}\frac{\partial p}{\partial \eta} - \mu_\mathrm{d}\right)}_{\substack{\text{net}\\ \text{vertical pressure}\\ \text{gradient}\\ \text{and buoyancy force}\\ \text{PGBUOY}_w}} + \underbrace{\left(\frac{uU + vV}{r_\mathrm{e}}\right)}_{\substack{\text{curvature}\\ \text{CUV}_w}} + \underbrace{D}_{\substack{\text{Rayleigh}\\ \text{damping}}} \tag{5}$$

where

$$-\nabla \cdot (\boldsymbol{V}a) = -\frac{\partial (Ua)}{\partial x} - \frac{\partial (Va)}{\partial y} - \frac{\partial (\Omega a)}{\partial \eta},$$

p is the full pressure with inclusion of water vapor, ϕ is the geopotential, r_e is the mean earth radius, and α and α_d are the full and dry-air specific volumes, respectively. For the horizontal momentum equations, the right-hand-side (rhs) forcing terms include the flux-form advection ($\mathrm{ADV}_{u,v}$), horizontal pressure gradient force (PGF_v; PGF_u=0 because $\frac{\partial}{\partial x} = 0$ in the 2D setup), Coriolis force ($\mathrm{COR}_{u,v}$), and earth-surface curvature ($\mathrm{CUV}_{u,v}$). For the w tendency in (5), the rhs forcings include the flux-form advection (ADV_w), net force between the vertical pressure gradient and buoyancy (PGBUOY_w), curvature effect (CUV_w) and the implicit Rayleigh damping for the vertical velocity (D), which can be neglected except at upper levels. Other parameterized terms may appear in these equations depending on the setup.

Budget analysis for (4)-(5) is conducted with an inline retrieval tool that strictly follows the model solver and thus has high accuracy with the 99th percentile of the residual always less than 0.1% of the concurrent tendency term (Chen et al. 2020). To demonstrate in a common physical unit (m s^{-2}), every term in the flux-form budget equation shown herein is divided by the dry-air mass μ_{d}. To facilitate CSI assessment, the geostrophic wind is diagnosed from the inline-retrieved PGF_{v}. However, the geostrophic wind field often appears noisier than the total wind, especially for small Δy (e.g., Shutts 1990). Thus, we applied the cowbell spectral filter (Barnes et al. 1996, Stoelinga 2009) to filter out gravity-wave-induced variations with a cutoff wavelength of 40 km on the u_{g} and M_{g} fields for $\Delta y \leq$10 km.

3.3 Initial conditions

An ideal design for a clean experiment for CSI is to construct an initial condition with uniform negative MPV_{g}^{*} or SCAPE in the domain. However, such a setup does not guarantee the absence of dry symmetric instability, conditional (static) or inertial instabilities. Moreover, a moisture field that satisfies these requirements may not be realistically distributed and would serve as an extra parameter affecting the flow dynamics. Thus, as in IC92 and PW95, we choose an iterative method to construct an initial flow by prescribing a constant zonal wind shear, $\frac{\partial u_{\mathrm{g}}}{\partial \mathrm{z}} = 5.8 \times 10^{-3}$ s^{-1}, a constant surface pressure of 1000 hPa, and horizontally uniform vertical profiles of Brunt–Väisälä frequency ($N^2 = \frac{g}{\theta_{\mathrm{v}}}\frac{\partial \theta_{\mathrm{v}}}{\partial z}$) and relative humidity (RH). By specifying the virtual potential temperature $\theta_{\mathrm{v}} = 287.5$ K at the surface on the southern boundary, we then solve for the hydrostatically balanced p, α, α_{d}, q_{v}, θ, and u_{g} for the entire domain. The resulting initial state contains horizontally uniform static stability ($N^2 > 0$) and baroclinicity ($f\frac{\partial u_{\mathrm{g}}}{\partial \mathrm{z}} > 0$), a constant inertial stability ($\frac{\partial M_{\mathrm{g}}}{\partial \mathrm{y}} < 0$), and decreasing CSI (in terms of the thickness of the $MPV_{\mathrm{g}}^{*} < 0$ layer in the lowest 4 km and SCAPE) from south to north (Fig. 1). CAPE is zero everywhere in the domain. The initial flow $(u, v, w) = (u_\mathrm{g}, 0, 0)$ is in thermal wind balance.

To initiate a single slantwise convective band, positive θ perturbations and negative u perturbations are added to the initial flow to provide locally positive buoyancy and inertial forces in the vertical and horizontal directions, respectively. Perturbations assume a bubble of the form

$$\Delta\varphi = \Delta\varphi_{\max}\cos^2(0.5\pi r) \quad \text{for } r \leq 1, \tag{6}$$

where φ represents θ or u, $r = \sqrt{(\frac{y-y_\mathrm{c}}{R})^2 + (\frac{z-z_\mathrm{c}}{H})^2}$, where $R = 50$ km and $H = 1.5$ km are the horizontal and vertical radii, respectively, and the center is located at $y_\mathrm{c} = 400$ km and $z_\mathrm{c} = 1.5$ km. The values of $\Delta\theta_{\max} = 0.5$ K and $\Delta u_{\max} = -6$ m s^{-1}, are chosen empirically to give just enough amplitude to trigger the release of CSI. This bubble is located where MPV_g^* is about -0.2 PVU and SCAPE is around 400 J kg^{-1} (Fig. 1b and c). This SCAPE value might seem small compared to characteristic values of CAPE during severe weather events, but it is reasonable in the context of the SCAPE climatology of Chen et al. (2018). To hasten CSI release while avoiding widespread slantwise convection developing in the domain, we also add an RH perturbation (to a maximum RH of 98.8%) over the area where the initial bubble is inserted (Fig. 1a). The step-by-step construction and the specified vertical profiles of N^2 and RH can be found in Appendix B of Chen et al. (2020).

4. Results

4.1 Overview of horizontal grid spacing sensitivity

We first provide an overview of the $\Delta y = 10$ km simulation to draw a comparison with past CSI studies using similar horizontal grid spacings. After the slantwise transverse circulation (v, w) is initiated, a slantwise band extends upward and northward with time (Fig. 2). The peak v and w are around 10 m s^{-1} and 20 cm s^{-1}, respectively. To avoid providing a misleading picture by outliers, the evolutions of their 99$^{\text{th}}$ percentiles are shown. These values peak at 5.3 m s^{-1} and 8.5 cm s^{-1} at around

21 h and 17 h, respectively (Fig. 2a). Compared to PW91's numerical study with a similar initial MPV_{g} of ~ -0.2 PVU (but calculated using the wet-bulb potential temperature instead of θ_{e}^{*}) and the same $\Delta y = 10$ km, our maximum (v, w) and the timescale are slightly larger and a few hours faster. However, the overall band evolution and life cycle are consistent. The simulated longer lifetime than the observed ~3-h CSI adjustment timescale in Reuter and Yau (1990) is possibly due to the lack of continuous external forcing in the idealized setup. The return flow is much more intense and deeper in the lower flank of the slantwise band than the upper side, consistent with PW91, PW95 and IC92 (Fig. 2b-c). During its development, the lower part of the band slowly drifts southward at a speed of about 1.2 m s^{-1}, similar in magnitude to that noted in IC92. The saturated band has a local width of several tens of km to 100 km, with the entire circulation extending over 400-500 km horizontally and from near the surface up to 8 km height at its peak intensity. SCAPE is reduced to nearly zero at some grid points where the return downdraft nearly reaches the surface (Fig. 2c). Since the initial condition is only weakly symmetrically unstable and the band develops in an unforced environment, the accumulated precipitation is modest with a local maximum of less than 2 mm over 20 h.

Figure 3 shows snapshots of the simulated slantwise circulation for all the experiments at 16 h. For $\Delta y =$40 km, the model fails to maintain the slantwise convection as the initial perturbation decays quickly, with almost no consequent reduction in SCAPE. Meanwhile, $\Delta y =$20 km only marginally resolves the band, resulting in a weak and slow growth.[2] The horizontal and vertical extents of the slantwise updraft are similar for $\Delta y = 1, 2, 5$ and 10 km. However, one obvious difference exists: instead of having one linearly-tilted band in $\Delta y =$10 km, an embedded quasi-

[2] Even with a wider initial perturbation, i.e., doubled R in (6), we obtain similar results. $\Delta y =$40 km still fails to maintain the band while $\Delta y =$20 km simulates a slower growth of slantwise band than the finer-grid simulations (not shown). Moreover, despite the doubled width of the initial perturbations, the developed slantwise band has similar width and thickness to the one with the original R.

upright cell develops at y$\sim$ 450 km and z =1.5-4 km for $\Delta y \leq 5$ km, breaking the slantwise band into two segments. Above this cell, the slantwise band continues to ascend with a gentler slope.

While the transient 99th percentile vertical velocity increases with finer horizontal grid spacing (Fig. 4a), the bulk features converge numerically at $\Delta y \leq 5$ km. These include the SCAPE consumption, accumulated precipitation and 48-hour averaged upward zonal momentum flux (Fig. 4b-d). For $\Delta y \leq 5$ km, around 100 J kg^{-1} of averaged SCAPE is consumed by 24 h, and the domain-averaged accumulated precipitation reaches 0.4 mm by 30 h. In contrast, the 10-km simulation shows much smaller effects (50 J kg^{-1} of SCAPE consumption and 0.2 mm of precipitation by 24 h and 30 h, respectively; Fig. 4b-c). The vertical profile of zonal momentum flux reflects an important large-scale feedback of the slantwise convection in baroclinic environments (Fig. 4d): the generally negative values indicate upward transport of the low zonal momentum and downward transport of high zonal momentum by the slantwise circulation. Simulations with coarser grid spacings exhibit a peak momentum flux at lower altitudes with smaller magnitudes than the finer-grid runs. As numerical bulk convergence is reached at $\Delta y = 5$ km, a robust peak magnitude of momentum flux of around -1.5×10^{-2} kg m^{-1} s^{-2} forms at $z = 4.5$ km.

The above results suggest that while $\Delta y = 10$ km is sufficient to simulate the general structure of the slantwise convection, the embedded quasi-upright convective cell that initiates at around 5 h for finer grid spacings may have significant impacts on the larger-scale environment, thus affecting whether or not the bulk properties numerically converge. Below we present evidence showing how the convective cell develops in an initially moist statically stable environment, how it then affects the slantwise band and the larger-scale environment differently between $\Delta y = 10$ km and ≤ 5 km runs.

4.2 Dynamical origin of the upright convection

The air parcel (tube) theory indicates that CSI can be released only if a finite-amplitude forcing is applied along a gentler angle than the sloped θ_e^* surfaces. Thus, positive θ_e^* advection must accompany the early initiation of the slantwise updraft. Although θ_e^* is not a prognostic variable, we have added an inline calculation for θ_e^* to WRF so that the θ_e^* advection can be estimated using the model's advection operator and the local θ_e^* tendency can be calculated inline (Chen et al. 2020). Because θ_e^* is only conserved for reversible moist adiabatic process in a saturated flow, irreversible processes (e.g., precipitation, mixing, etc.) and diabatic processes can regulate its distribution. Nevertheless, Fig. 5 shows that the advection still dominates the local θ_e^* tendency, at least in the vicinity of the slantwise band.

During the early development of the slantwise convection, the differential advection of θ_e^* between the updraft and the surrounding environment renders θ_e^* surfaces buckled (i.e., distorted) locally (Fig. 5c-d), leading to the formation of conditional instability (i.e., $\frac{\partial \theta_e^*}{\partial z} < 0$) (e.g., Bennetts and Hoskins 1979, Bennetts and Sharp 1982, IC92, PW95). A shallow layer of conditional instability develops above the maximum ascent by 5 h (Fig. 5c-d). As the slantwise band extends upward, the updraft penetrates this conditionally unstable layer, which splits into two at about 7 h (not shown). While the conditionally unstable layer remains intact for Δy=10 km at later times, it breaks up into small scattered patches in $\Delta y \leq 5$ km with stronger *w*, indicating a stronger release of conditional instability in the latter (Fig. 5g-h; similar features shown for Δy=5 km are also observed for Δy <5 km). Note that at 9 h, strong θ_e^* tendencies with opposite signs stacking below the head of the slantwise band likely reflect the inertia-gravity waves triggered by the slantwise convection, forming in response to weak ageostrophy in a sheared environment (Fig. 5g-h; PW95, Huang 1991). Despite the transient large magnitudes, these waves do not have long-lasting impacts locally as the environment recovers after they propagate away (not shown).

The inline budget analysis of w tendency equation (5) shows that the positive PGBUOY_w along the slantwise ascent is already slightly stronger and wider for $\Delta y \leq 5$ km than for $\Delta y = 10$ km at 5 h (not shown). This term represents the transient imbalance between the buoyancy and vertical gradient of pressure perturbation, indicating the non-hydrostatic forcing. While the PGBUOY_w is maximized at about 1.5×10^{-5} m s^{-2} for $\Delta y = 10$ km, $\Delta y \leq 5$ km exhibits peak values of above 6.5×10^{-5} m s^{-2} at 7 h (Fig. 6d-f; note that the budget analysis for $\Delta y = 2$ km is also presented to help access the degree of numerical convergence for $\Delta y \leq 5$ km). By 9 h, the maximum PGBUOY_w in $\Delta y \leq 5$ km is ten times larger than that in $\Delta y = 10$ km over the area where conditional instability previously existed (not shown). It is a well-known relationship that stronger PGBUOY_w develops at smaller Δy because, for a given buoyancy, the opposing vertical PGF weakens as the scale of the circulation contracts, leading to stronger non-hydrostatic acceleration. This can be inferred from the linear dispersion relation (Orlanski 1981), which shows that given the same degree of convective instability, the growth rate of the unstable waves increases with reducing Δy in the mesoscale for $H/\Delta y \lesssim 1$, where H is the vertical scale of the motion. In the present case, although $\Delta y = 10$ km captures the overturning of θ_{e}^{*} surfaces (Fig. 5c; also for $\Delta y = 20$ km (not shown)), such Δy is too coarse to allow the instability to grow at a realistic rate. Notably, even without adequately resolving the transient non-hydrostatic forcing for the embedded convective cell, $\Delta y = 10$ km still reasonably captures the general feature of the slantwise band (Fig. 3d). This indicates that the hydrostatic forcing (buoyancy) is still highly dominant for the general slantwise convection, with buoyancy ($O(10^{-2}$ m s^{-2}); not shown) being three orders of magnitude larger than the non-hydrostatic forcing even for $\Delta y \leq 5$ km. The non-hydrostatic forcing is weak, as one would expect given the shallow and weak conditional instability, but is nevertheless responsible for accelerating the embedded convective cell differently between finer-grid and coarse-grid simulations.

For $\Delta y \leq 5$ km, the major upright convection persists until ~24 h but is confined to low levels even at later stages of the slantwise convection development (not shown). This is because the layer with $MPV_{\mathrm{g}}^{*} < 0$, i.e., where θ_{e}^{*} surfaces are steeper than M_{g} surfaces, does not extend beyond 4 km (Fig. 1b). Thus, although the slantwise band continues to grow upward at the expense of SCAPE, the slope of the ascent becomes parallel and even steeper than the surrounding θ_{e}^{*} surfaces, and thus the associated θ_{e}^{*} advection does not lead to strongly buckled/overturned θ_{e}^{*} contours at upper levels.

4.3 Early-staged evolution of the slantwise circulation

To obtain a more comprehensive picture of the evolution of w in slantwise convection, other contributing processes in (5) must also be examined. This section focuses on the early stage of the slantwise development before 9 h. While strongly positive PGBUOY_w mainly occurs over the upright convective core, the earth-surface curvature (CUV_w) is positive everywhere with increasing values with height. CUV_w is dominated by the (re-)distribution of zonal momentum, and so areas with small values extend upward as the growing slantwise band, which do not show an obvious sensitivity to Δy (Fig. 6g-i). Meanwhile, the advection term (ADV_w) shows differences as early as 4 h, with the $\Delta y =$10 km case exhibiting generally weaker magnitudes and a maximum located more northward rather than upward than for $\Delta y \leq 5$ km (e.g., Fig. 6a-c). These differences increase with time as the updraft core intensifies more strongly with a more vertically tilted axis, leading to stronger horizontal gradient of w and thus stronger ADV_w for $\Delta y \leq 5$ km. ADV_w generally reaches the same order of magnitude but with opposite signs as the net driving force of $\mathrm{PGBUOY}_w + \mathrm{CUV}_w$ (Fig. 6a-c and j-l). The combined total tendency thus has peak values shifted northward and upward from where the $\mathrm{PGBUOY}_w + \mathrm{CUV}_w$ is largest, indicating the upward and northward propagation of the developing slantwise band (Fig. 6m-o).

The dynamical sensitivities to the grid spacing are also reflected in the meridional motions, in which the inertial force (PGF_v+COR_v) is crucial in driving slantwise convection. In the initially geostrophically balanced background flow, PGF_v and COR_v point north (i.e., positive) and south (i.e., negative), respectively (Fig. 7d-i). The initial introduction of a negative u perturbation causes COR_v to no longer fully oppose PGF_v, which gives rise to a positive acceleration to the north. During the continuous release of CSI, such positive inertial forces are sustained over time, expand in area, and strengthen locally, fueling the v circulation for several hours (Fig. 7j-l). This is largely owing to the slantwise ascent transporting smaller u from lower levels upward and thus locally reducing the magnitude of COR_v (i.e., fu) along the sloped updraft (Fig.7g-i). Such a self-maintaining mechanism has been documented in past studies (e.g., IC92, PW93).

Although the evolution of PGF_v in slantwise convection has not been extensively studied, it shows a larger sensitivity to Δy than does COR_v (Fig.7d-f). IC92 considered that warming via positive θ_e advection and the condensational heating would lead to a local hydrostatic pressure drop maximized in the central part of the updraft. This pressure change would result in a pair of PGF_v anomalies that act in the opposite direction, slightly reducing and reinforcing the northward acceleration on the northern and southern half of the band, respectively. They view this pair of PGF_v anomalies as responsible for the observed slow drift of the slantwise updraft toward the warmer side of the domain while the parcels themselves move toward the north. However, our inline-budget-retrieval results show a much more complicated quantitative picture than the conceptual one in IC92.

Generally speaking, PGF_v contributes negatively to the evolution of inertial force as the area with weakening (i.e., less positive) PGF_v extends upward as the band grows (Fig. 7d-f). Comparing the distribution of COR_v and PGF_v suggests that the sustaining positive inertial force over the slantwise ascent is mainly due to the less-negative COR_v overpowering the less-positive PGF_v (Fig.

7d-l). However, the broadly distributed PGF_v can have dominant effects outside of the slantwise ascent. Specifically, PGF_v exhibits weaker values over a wide isosceles-triangular region covering from the top of slantwise band to the surface, and so a negatively-tilted patch of negative inertial force develops below the band (e.g., Fig. 7d-f and j-l). This explains the deeper and more intense return flow in the lower flank than the upper side of the slantwise convection (Fig. 2). To the north of the triangular area, strong PGF_v overpowers COR_v, leading to positive inertial force enhancement that helps the upper-northern part of the slantwise band accelerate northward.

Compared to $\Delta y = 10$ km, the PGF_v feature in $\Delta y \leq 5$ km is more pronounced, exhibiting a more vertically oriented spatial distribution with smaller values reaching higher altitudes and a slightly stronger PGF_v to its north (Fig. 7d-f). On one hand, the negatively-tilted negative inertial force can penetrate the v core, tending to break the v contours into two segments across the convective cell. This results in a detached instead of linearly-tilted slantwise band at finer grids (Fig. 3). On the other hand, the locally stronger PGF_v accelerates v of the detached upper band much more so for $\Delta y \leq 5$ km than for $\Delta y = 10$ km (Fig. 7j-l). To sum up, the weakening of the south-pointing COR_v is critical for sustaining and accelerating the horizontal motion over the slantwise ascent region as the north-pointing PGF_v is generally weakening there. Meanwhile, the localized strengthening of PGF_v, especially to the north of the w core (Figs. 6a-c and 7d-f), accelerates and extends the upper-northern part of the slantwise band northward. While the COR_v evolution does not show a significant grid-spacing sensitivity at the early stage, the PGF_v effect becomes more pronounced at finer grids.

4.4 Maintenance of the slantwise band and its large-scale feedbacks

As upright convection lasts, it transports more low zonal momentum upwards and thus increases the imbalance between PGF_v and COR_v at upper levels while the inertial force weakens at lower levels (Fig. 8). A locally strengthened inertial force above the upright convection has been observed over both squall lines and frontal regions (Zhang and Cho 1992, Browning et al. 2001). Here, the apparently stronger inertial force over the upper slantwise band in $\Delta y \leq 5$ km (relative to the $\Delta y = 10$ km case) lasts until 20 h, causing v contours with gentler slopes there (Fig. 8).

Having examined the detailed dynamics during the evolution of slantwise convection, we return to their links to the large-scale feedbacks. Recalling Fig. 4, a question remains as to how exactly does the better-resolved upright-convection-associated features in $\Delta y \leq 5$ km contribute to the faster and stronger neutralization of CSI, i.e., larger release of environmental SCAPE, hence leading to larger precipitation and vertical momentum fluxes than the coarser-gridded simulations? Although both θ_{e}^{*} and M_{g} surfaces become buckled locally during the development, the later state when the CSI circulation is about to cease shows that the slopes of the θ_{e}^{*} surfaces change more than that of the M_{g} surfaces from their initial states (Fig. 9). The θ_{e}^{*} surfaces become flattened not only over the region traversed by the slantwise band but also in the column below. In the example given in Fig. 9, for an air tube lifted from the surface at y ~400 km, the flattened θ_{e}^{*} surfaces become increasingly parallel to the M_{g} surfaces over time and lower the LSNB by 1-2 kilometers by 24 h. These factors lead to a smaller surface integral between the θ_{e}^{*} and M_{g} surfaces at the later time, and thus smaller SCAPE for air tubes initialized at the same near-surface location.

The more parallel θ_{e}^{*} and M_{g} surfaces in $\Delta y \leq 5$ km than $\Delta y = 10$ km are especially noticeable at low levels. While both $\Delta y \leq 5$ km and $\Delta y = 10$ km capture the strong θ_{e}^{*} increase over the lower flank of the slantwise band as some cross-θ_{e}^{*} return flow brings the higher-θ_{e}^{*} downward, enhanced low-level warming only occurs in $\Delta y \leq 5$ km (Fig. 10). This warming is caused by the continuous positive vertical θ_{e}^{*} advection due to the descending flow associated with the resolved upright convection (Fig. 10 d-e). Meanwhile, for $\Delta y = 10$ km, the sloped downdraft becomes mostly parallel to the surrounding θ_e^* surfaces at low-to-middle levels (Fig. 10a-b). While the evaporative cooling of precipitation partially offsets the warming in the lowest 2 km, a patch of positive θ_e^* anomaly persists between 1.5~3.5 km in $\Delta y \leq 5$ km even after the upright convection weakens (Fig. 10f). Thus, adequately resolving upright convection formed by the early-stage slantwise motion can have a major impact on the CSI release and corresponding moist-symmetric stabilization.

5. Additional sensitivity tests and potential limitations

5.1 Vertical grid spacing

Because the local thickness of the slantwise band can be small in a convectively stable environment (as shown here and in PW93), a high vertical resolution is needed to adequately resolve it. PW93 suggested $\Delta z \leq 170$ m and we used $\Delta z \leq 125$ m for all simulations. Another issue worthy of consideration is that when the horizontal and vertical grid spacings are not changed consistently, spurious gravity waves, appearing as short-wavelength variations, might be generated (PW91). This is particularly important for simulating a narrow sloping thermal feature because resolving the slope depends on the ratio of Δy and Δz, which may result in a discontinuous "stairs-like" feature that introduces perturbations into the mass field (Lindzen and Fox-Rabinovitz 1989). Huang's (1999) numerical study on slantwise convection with a fixed $\Delta y = 10$ km but different vertical grid spacings also supports this finding. PW91 proposed the following guideline to mitigate such effects:

$$\mathrm{AS} \leq 1, \qquad \text{where } \mathrm{AS} \equiv \frac{\Delta p/\Delta y}{s}, \tag{7}$$

Δp and Δy are the grid spacings in pressure coordinates and horizontal grid length, respectively, and s is the slope of the slantwise/frontal structure on (p, y) coordinates. In our simulations, (7) is satisfied for all the simulations with $\Delta y \geq 5$ km.

To test whether our finer-grid simulations are affected by the inconsistent horizontal and vertical grid length, we carried out additional simulations with an increased vertical resolution to

320 and 640 levels for Δy =2 and 1 km, respectively (both result in an AS~0.96, as in the 5-km run). In those simulations, the convective features within the slantwise updraft do not change significantly and the fields sometimes appear even nosier outside of the primary band than for their coarser vertically gridded counterparts. The inconsistency between this result and those of PW91 and Huang (1991) may be caused by other factors (physical and/or spurious) that were absent in both past studies with a horizontal resolution of 10 km, namely increased upright convection owing to the buckling of θ_e^* surfaces and the presence of non-hydrostatic dynamics.

5.2 Tests with cumulus parameterization schemes

Our results suggest that the ability to resolve embedded upright convection has important impacts on the CSI neutralization process. It is therefore of interest to know whether the inclusion of available parameterization schemes for upright convection can bring the $\Delta y = 10$ km simulation closer to the converged results for $\Delta y \leq 5$ km. Two different convective schemes are tested. In a 10 km-simulation with the Kain-Fritsch scheme (Kain 2004), the deep convection parameterization is never activated due to the shallowness of the convective layer. Another test for $\Delta y = 10$ km uses the Tiedtke scheme (Zhang et al. 2011), which shows a minor enhancement in the total precipitation starting from the beginning of the simulation, but it does not appear to be physically associated with the slowly developing slantwise band as simulated in $\Delta y = 5$ km (not shown). The rest of the bulk properties (i.e., SCAPE and upward momentum flux) also do not change significantly (not shown). These results suggest that, although the upright convective cell is the key feature differentiating the coarser- and finer-grid simulations, the use of existing upright convective parameterizations at coarser resolution does not necessarily improve the representation of this feature.

5.3 Generality of the embedded upright convection

Although the results presented herein are derived from a single idealized setup, embedded upright convective cells are believed to be general features during the development of slantwise convection. The parcel (tube) theory guarantees that CSI release must be accompanied by some degree of positive θ_e^* advection. Whether this advection can induce the overturning of θ_e^* surfaces, i.e., $\frac{\partial \theta_e^*}{\partial z}<0$, depends on the environmental stability and the strength and vertical slope of the circulation. For weaker stabilities and stronger ascent rates, both of which are associated with more intense and meteorologically significant slantwise bands, the probability of this overturning is particularly high. The formation of convective instability above a developing slantwise band has been extensively documented in both observational and numerical studies (e.g., Bennetts and Hoskins 1979, Bennetts and Sharp 1982, Thorpe and Clough 1991, IC92, PW95).

5.4 Limitations of the 2D framework

Strictly speaking, symmetric instability theory is applicable only to two-dimensional flow. However, real-world slantwise bands have 3D structures such as a finite length and some variability along the direction of symmetry (the thermal wind direction; x), partially due to the chaotic nature of atmosphere with turbulence, non-symmetric environmental conditions, etc. Jones and Thorpe (1992) investigated the 3D nature of slantwise band by considering two possible situations in a 3D model: (a) the region with CSI is assumed 2D, i.e., extending infinitely along x, but the trigger to release the instability occurs only locally; or (b) the region that contains CSI has a finite length in x. Both scenarios result in circulations that gradually become more elongated in x, forming the quasi-linear but finite-length banded structure with some degrees of horizontal tilt/orientation from x. They found that the magnitude and direction of this tilt are associated with the viscous properties of the flow. Interestingly, the growth rate in scenario (b) depends on a ratio of the length of the CSI region in x and the horizontal wavelength of the circulations in y (along temperature gradient). The longer the CSI region is in x, the larger the corresponding slantwise growth rate. Thus, for CSI to occur in the 3D world, there exist minimum thresholds in both the width and length of the CSI region.

Other caveats in the 2D framework could arise from the deficiency of the 2D model in representing the realistic 3D physics. One example is that 2D models generally provide a poor representation of 3D atmospheric turbulence. Zhang and Cho (1995) conducted a 3D simulation of an Eady wave, building on an earlier 2D study of Knight and Hobbs (1988). They documented the differences introduced by the inclusion of the third spatial dimension, such as the curving features of the quasi-linear rainbands and their 8-10 degrees deviations from the along-front (i.e., x) direction. Moreover, 2D models tend to simulate updrafts that lean downshear, leading to weaker growth of the slantwise band. They associated this problem to the unrealistic representation of divergence, vortex stretching, and tilting in 2D models when environmental wind shears are strong. Nevertheless, as in Jones and Thorpe (1992), their 3D simulated results conformed in many aspects to the CSI theory and its 2D interpretations.

6. Conclusions

Recent climatological studies have reinforced the potential global importance of slantwise convection, raising questions about whether large-scale models can resolve slantwise convection and under what conditions should it be parameterized. To address these questions, the present study simulates isolated free moist slantwise convection (the process by which conditional symmetric instability, or CSI, is released without continuous external forcings) in a baroclinic environment that is initially unstable to slantwise displacements but inertially and conditionally stable. The simulations are conducted in an idealized, non-hydrostatic, 2D (y–z plane) framework with the Weather Research and Forecasting (WRF) model. The sensitivities of the slantwise convection to the horizontal (cross-band; along the temperature gradient) grid spacing (Δy; varied from 40, 20, 10, 5, 2 to 1 km) are examined to determine the necessary grid spacing to robustly capture the band dynamics and larger-scale feedbacks. While $\Delta y = 40$ and 20 km are too coarse to sustain the slantwise circulation, $\Delta y = 10$ km can reasonably capture its general feature, including the spatial extent (i.e., 400-500 km horizontally and 8 km vertically) and the timescale to reach peak intensity. However, the slantwise-convection-associated large-scale impacts are found to converge numerically at $\Delta y \leq 5$ km. We utilize an inline momentum-budget retrieval method to identify the dynamical processes that account most for the grid-spacing sensitivity.

We found that the key feature that differentiates the converged and non-converged bulk properties is closely related to a major upright convective cell that emerge within the slantwise band at low levels only for $\Delta y \leq 5$ km. The upright cell develops when the growing sloped updraft enters a shallow conditionally unstable layer, which forms at around 4-5 h due to the strong positive θ_{e}^{*} advection by the developing slantwise ascent itself. The w-budget shows that $\Delta y \leq 5$ km can resolve the localized convective cell better, releasing conditional instability with an order-of-magnitude stronger non-hydrostatic force (i.e., imbalance between the vertical pressure gradient and buoyancy; PGBUOY_w) than $\Delta y = 10$ km.

As for the horizontal flow of the slantwise band, the v acceleration depends on the inertial force, i.e., imbalance between the horizontal pressure gradient force (PGF_v; initially positive toward the north) and the Coriolis force (COR_v; initially negative toward the south). COR_v plays a self-sustaining role in the slantwise convection evolution as it becomes less negative while slantwise ascent transporting lower zonal momentum u upward. The changes of PGF_v exhibit a more complicated spatial distribution. On one hand, the widespread weakening PGF_v leads to a reversed inertial force extending to the surface which is responsible for the deep and intense return flow over the lower flank of the slantwise ascent. While COR_v shows a relatively small grid-spacing sensitivity at the early stage, PGF_v exhibits a more distinctive feature at finer grids. The weakening PGF_v at low levels can penetrate the slantwise ascent and break the v contours across the embedded convective cell for $\Delta y \leq 5$ km. On the other hand, the localized strengthening of PGF_v to the north of maximum updraft becomes more pronounced at finer grids, leading to a stronger northward acceleration and extension of the upper-level (detached) band than the coarser-grid runs.

The resolved upright convection promotes a faster release of CSI. The embedded upright convective cell in finer-grid simulations continuously transports more air with low u upward, leading to a stronger inertial force that enhances the northward accelerations at upper levels. Moreover, the descending cross-θ_e^* flow associated with the upright convective cell strengthens the positive θ_e^* advection beneath the slantwise updraft, causing additional warming of θ_e^* at low levels for $\Delta y \leq 5$ km. This warming helps flatten θ_e^* surfaces to be closer to geostrophic absolute momentum (M_g) surfaces and lower the level of slantwise neutral buoyancy, resulting in a larger consumption of slantwise convective available potential energy (SCAPE), i.e., larger adjustment toward a slantwise-neutral state. Therefore, accumulated precipitation and the domain-averaged vertical momentum flux both increase in magnitude with decreasing Δy until 5 km is reached. While this study shows that the smaller-scale upright convective processes can have significant impacts on the larger-scale environments, we reiterate that slantwise convection itself is still dominantly driven by the hydrostatic forcing (buoyancy; which is three orders of magnitude larger than the non-hydrostatic forcing), and therefore $\Delta y = 10$ km can still reasonably capture its general feature.

The current findings suggest that numerical models may not adequately resolve critical properties associated with the development of slantwise convection with a horizontal grid spacing coarser than around 5 km. Because slantwise convection can exist in an environment without CAPE (as shown herein), existing parameterizations for upright convection may not properly capture it. Thus, either these schemes should be adapted to account for slantwise convection and its larger-scale feedbacks, or new schemes for pure slantwise convection should be developed (e.g., Emanuel 1983a, PW93, Schultz and Schumacher 1999). A few studies (e.g., Lindstrom and Nordeng 1992, Balasubramanian and Yau 1995, Ma 2000) have shown that inclusion of slantwise convective parameterization in numerical models improves forecasts of precipitation, jet, and/or cyclone intensity, but these schemes have not been commonly employed. Chang et al. (2013) and Zappa et al. (2013) compared the historical simulations from the phase 3 and 5 of the Coupled Model Intercomparison Project (CMIP3 and CMIP5) with the reanalysis data, respectively, and both found significant biases in extratropical storm tracks properties. Considering that slantwise convection is climatologically important in the midlatitudes (e.g., Glinton et al. 2017), particularly for rapidly deepening cyclones (Chen et al. 2018), implementing a slantwise convection parameterization in climate models may be beneficial for their general forecast skill.

References

Baker, L. H., Gray, S. L. and Clark, P. A. (2014) Idealised simulations of sting-jet cyclones. *Q.J.R. Meteorol. Soc.*, **140**, 96-110, https://doi.org/10.1002/qj.2131.

Balasubramanian, G. and Yau, M. K. (1994a) Baroclinic instability in a two-layer model with parameterized slantwise convection. *J. Atmos. Sci.*, **51**, 971-990, https://doi.org/10.1175/1520-0469(1994)051<0971:BIIATL>2.0.CO;2.

—— and —— (1994b) The effects of convection on a simulated marine cyclone. *J. Atmos. Sci.*, **51**, 2397–2417, https://doi.org/10.1175/1520-0469(1994)051<2397:TEOCOA>2.0.CO;2.

—— and —— (1995) Explosive marine cyclogenesis in a three-layer model with a representation of slantwise convection: a sensitivity study. *J. Atmos. Sci.*, **52**, 533–550, https://doi.org/10.1175/1520-0469(1995)052<0533:EMCIAT>2.0.CO;2.

Barnes, S. L., Caracena, F., and Marroquin, A. (1996) Extracting synoptic-scale diagnostic information from mesoscale models: The Eta model, gravity waves, and quasigeostrophic diagnostics. *Bull. Amer. Meteor. Soc.*, **77**, 519–528, https://doi.org/10.1175/ 1520-0477(1996)077,0519:ESSDIF.2.0.CO;2.

Bélair, S. and Mailhot, J. (2001) Impact of horizontal resolution on the numerical simulation of a midlatitude squall line: implicit versus explicit condensation. *Mon. Wea. Rev.*, **129**, 2362–2376, https://doi.org/10.1175/1520-0493(2001)129<2362:IOHROT>2.0.CO;2.

Bennetts, D. A. and Hoskins, B. J. (1979) Conditional symmetric instability - a possible explanation for frontal rainbands. *Q.J.R. Meteorol. Soc.*, **105**, 945-962, https://doi.org/10.1002/qj.49710544615.

—— and Sharp, J. C. (1982) The relevance of conditional symmetric instability to the prediction of mesoscale frontal rainbands. *Q.J.R. Meteorol. Soc.*, **108**, 595-602, https://doi.org/10.1002/qj.49710845707.

Browning, K. A., Chapman, D. and Dixon, R. S. (2001) Stacked slantwise convective circulations. *Q.J.R. Meteorol. Soc.*, **127**, 2513-2536, https://doi.org/10.1002/qj.49712757803.

Chang, E. K. M., Guo, Y., Xia, X., and Zheng, M. (2013) Storm-Track Activity in IPCC AR4/CMIP3 Model Simulations. *J. Climate*, **26**, 246–260, https://doi.org/10.1175/JCLI-D-11-00707.1.

Chen, T.-C., Yau, M.K. and Kirshbaum, D.J. (2018) Assessment of conditional symmetric instability from global reanalysis data. *J. Atmos. Sci.*, **75**, 2425–2443, https://doi.org/10.1175/JAS-D-17-0221.1.

——, —— and —— (2020) Towards the closure of momentum budget analyses in the WRF (v3.8.1) model, *Geosci. Model Dev.*,**13**, 1737-1761, https://doi.org/10.5194/gmd-13-1737-2020.

Dixon, R. S., Browning, K. A. and Shutts, G. J. (2002) The relation of moist symmetric instability and upper-level potential-vorticity anomalies to the observed evolution of cloud heads. *Q. J. R. Meteorol. Soc.*, **128**, 839-859, https://doi.org/10.1256/0035900021643719.

Emanuel, K. A. (1983a) The Lagrangian parcel dynamics of moist symmetric instability. *J. Atmos. Sci.*, **40**, 2368–2376, https://doi.org/10.1175/1520-0469(1983)040,2368:TLPDOM.2.0.CO;2.

—— (1983b) On assessing local conditional symmetric instability from atmospheric soundings. *Mon. Wea. Rev.*, **111**, 2016–2033, https://doi.org/10.1175/1520-0493(1983)111,2016:OALCSI.2.0.CO;2.

—— (1988) Observational evidence of slantwise convective adjustment. *Mon. Wea. Rev.*, **116**, 1805-1816, https://doi.org/10.1175/1520-0493(1988)116<1805:OEOSCA>2.0.CO;2.

—— (1994) Slantwise convection. *Atmospheric Convection.* Oxford University Press. 580 pp.

Glinton, M. R., Gray, S. L., Chagnon, J. M. and Morcrette, C. J. (2017) Modulation of precipitation by conditional symmetric instability release. *Atmos. Res.*, **185**, 186-201, https://doi.org/10.1016/j.atmosres.2016.10.013.

Gray, S. L. and Thorpe, A. J. (2001) Parcel theory in three dimensions and the calculation of SCAPE. *Mon. Wea. Rev.*, **129**, 1656–1672, https://doi.org/10.1175/1520-0493(2001)129<1656:PTITDA>2.0.CO;2.

——, Martínez-Alvarado, O., Baker, L. H. and Clark, P. A. (2011) Conditional symmetric instability in sting-jet storms. *Q.J.R. Meteorol. Soc.*, **137**, 1482-1500, https://doi.org/10.1002/qj.859.

Hoskins, B. J. (1974) The role of potential vorticity in symmetric stability and instability. *Q.J.R. Meteorol. Soc.*, **100**, 480-482, https://doi.org/10.1002/qj.49710042520.

Huang, J. (1991) A numerical study of slantwise convection. M.S. thesis, Dept. of Atmospheric and Oceanic Sciences, McGill University, 73pp.

Innocentini, V. and Dos Santos Caetano Neto, E. (1992) A numerical study of the role of humidity in the updraft driven by moist slantwise convection. *J. Atmos. Sci.*, **49**, 1092–1106, https://doi.org/10.1175/1520-0469(1992)049<1092:ANSOTR>2.0.CO;2.

Jiang, H. and Raymond, D. J. (1995) Simulation of a mature mesoscale convective system using a nonlinear balance model. *J. Atmos. Sci.*, **52**, 161–175, https://doi.org/10.1175/1520-0469(1995)052<0161:SOAMMC>2.0.CO;2.

Jones, S.C. and Thorpe, A.J. (1992), The three-dimensional nature of ‘symmetric’ instability. *Q.J.R. Meteorol. Soc.*, 118, 227-258. https://doi.org/10.1002/qj.49711850404.

Kain, J. S. (2004) The Kain–Fritsch convective parameterization: an update. *J. Appl. Meteor.*, **43**, 170–181, https://doi.org/10.1175/1520-0450(2004)043<0170:TKCPAU>2.0.CO;2.

Klemp, J. B., Dudhia, J. and Hassiotis, A.D. (2008) An upper gravity-wave absorbing layer for NWP applications. *Mon. Wea. Rev.*, **136**, 3987–4004, https://doi.org/10.1175/2008MWR2596.1.

Knight, D. J., and Hobbs, P. V. (1988) The mesoscale and microscale structure and organization of clouds and precipitation in mid-latitude cyclones. Part XV: a numerical modeling study of frontogenesis and cold-frontal rainbands. *J. Atmos. Sci.*, **45**, 915–930, https://doi.org/10.1175/1520-0469(1988)045<0915:TMAMSA>2.0.CO;2.

Kuo, Y., Shapiro, M. A. and Donall, E. G. (1991) The interaction between baroclinic and diabatic processes in a numerical simulation of a rapidly intensifying extratropical marine cyclone. *Mon. Wea. Rev.*, **119**, 368–384, https://doi.org/10.1175/1520-0493(1991)119<0368:TIBBAD>2.0.CO;2.

Lean, H. W. and Clark, P. A. (2003) The effects of changing resolution on mesoscale modeling of line convection and slantwise circulations in FASTEX IOP16. *Q.J.R. Meteorol. Soc.*, **129**, 2255-2278. https://doi.org/10.1256/qj.02.57.

Lindstrom, S. S. and Nordeng, T. E. (1992) Parameterized slantwise convection in a numerical model. *Mon. Wea. Rev.*, **120**, 742–756, https://doi.org/10.1175/1520-0493(1992)120<0742:PSCIAN>2.0.CO;2.

Lindzen, R. S. and Fox-Rabinovitz, M. (1989) Consistent vertical and horizontal resolution. *Mon. Wea. Rev.*, **117**, 2575–2583, https://doi.org/10.1175/1520-0493(1989)117<2575:CVAHR>2.0.CO;2.

Ma, L. (2000) On the parameterization of slantwise convection in general circulation models. Ph.D. thesis, Dept. of Atmospheric and Oceanic Sciences, McGill University, 175 pp.

Markowski, P. M. and Richardson, Y. P. (2010) *Mesoscale meteorology in midlatitudes.* Wiley-Blackwell, 424 pp.

Orlanski, I. (1981) The quasi-hydrostatic approximation. *J. Atmos. Sci.*, **38**, 572–582, https://doi.org/10.1175/1520-0469(1981)038%3c0572:TQHA%3e2.0.CO;2.

Ooyama, K. (1966) On the stability of the baroclinic circular vortex: a sufficient criterion for instability. *J. Atmos. Sci.*, **23**, 43–53, https://doi.org/10.1175/1520-0469(1966)023<0043:OTSOTB>2.0.CO;2.

Persson, P. O. and Warner, T. T. (1991) Model generation of spurious gravity waves due to inconsistency of the vertical and horizontal resolution. *Mon. Wea. Rev.*, **119**, 917–935, https://doi.org/10.1175/1520-0493(1991)119<0917:MGOSGW>2.0.CO;2.

—— and —— (1993) Nonlinear hydrostatic conditional symmetric instability: implications for numerical weather prediction. *Mon. Wea. Rev.*, **121**, 1821–1833, https://doi.org/10.1175/1520-0493(1993)121<1821:NHCSII>2.0.CO;2.

—— and —— (1995) The nonlinear evolution of idealized, unforced, conditional symmetric instability: A numerical study. *J. Atmos. Sci.*, **52**, 3449–3474, https://doi.org/10.1175/1520-0469(1995)052<3449:TNEOIU>2.0.CO;2.

Reuter, G. W. and Yau, M. K. (1990) Observations of slantwise convective instability in winter cyclones. *Mon. Wea. Rev.*, **118**, 447–458, https://doi.org/10.1175/1520-0493(1990)118<0447:OOSCII>2.0.CO;2.

—— and —— (1993) Assessment of slantwise convection in ERICA cyclones. *Mon. Wea. Rev.*, **121**, 375–386, https://doi.org/10.1175/1520-0493(1993)121<0375:AOSCIE>2.0.CO;2.

Schultz, D.M. and Schumacher, P.N. (1999) The use and misuse of conditional symmetric instability. *Mon. Wea. Rev.*, **127**, 2709–2732, https://doi.org/10.1175/1520-0493(1999)127<2709:TUAMOC>2.0.CO;2.

—— and Browning, K. (2017) What is a sting jet? *Weather*. **72**, 63-66, https://doi.org/10.1002/wea.2795.

Seman, C.J. (1994) A numerical study of nonlinear nonhydrostatic conditional symmetric instability in a convectively unstable atmosphere. *J. Atmos. Sci*., **51**, 1352–1371, https://doi.org/10.1175/1520-0469(1994)051<1352:ANSONN>2.0.CO;2.

Sherwood, S. C. (2000) On moist instability. *Mon. Wea. Rev.*, **128**, 4139-4142, https://doi.org/10.1175/1520-0493(2000)129<4139:OMI>2.0.CO;2.

Shutts, G.J. (1990) SCAPE chars from numerical weather prediction model fields. *Mon. Wea. Rev.*, **118**, 2745-2751, https://doi.org/10.1175/1520-0493(1990)118<2745:SCFNWP>2.0.CO;2.

Skamarock, W. C., Klemp, J. B., Dudhia, J., Gill, D. O., Barker, D. M., Duda, M. G, Huang, X.-Y., Wang, W., and Powers, J. G. (2008) A description of the advanced research WRF version 3. *NCAR Tech. Note NCAR/TN-475+STR*, 113 pp, https://doi.org/10.5065/D68S4MVH.

Stoelinga, M. T. (2009) A users guide to RIP version 4.6: A program for visualizing mesoscale model output, https://a.atmos.washington.edu/~ovens/ripug_uw.html.

Stull, R. B. (1991) Static stability- an update. *Bull. Amer. Meteor. Soc.*, **72**, 1521-1529, https://doi.org/10.1175/1520-0477(1991)072<1521:SSU>2.0.CO;2.

Thompson, G., Field, P. R., Rasmussen, R. M., Hall, W. D. (2008) Explicit forecasts of winter precipitation using an improved bulk microphysics scheme. Part II: implementation of a new snow parameterization. *Mon. Wea. Rev.*, **136**, 5095–5115, https://doi.org/10.1175/2008MWR2387.1.

Thorpe, A. J. and Rotunno, R. (1989) Nonlinear aspects of symmetric instability. *J. Atmos. Sci.*, **46**, 1285–1299, https://doi.org/10.1175/1520-0469(1989)046<1285:NAOSI>2.0.CO;2.

—— and Clough, S. A. (1991) Mesoscale dynamics of cold fronts: structures described by dropsoundings in FRONTS 87. *Q.J.R. Meteorol. Soc.*, **117**, 903-941, https://doi.org/10.1002/qj.49711750103.

Wicker, L.J. and Skamarock, W.C. (2002) Time-splitting methods for elastic models using forward time schemes. *Mon. Wea. Rev.*, **130**, 2088–2097, https://doi.org/10.1175/1520-0493(2002)130<2088:TSMFEM>2.0.CO;2.

Xu, Q. (1986) Conditional symmetric instability and mesoscale rainbands. *Q.J.R. Meteorol. Soc.*, **112**, 315-334, https://doi.org/10.1002/qj.49711247203.

Zappa, G., Shaffrey, L. C., and Hodges, K. I. (2013) The ability of CMIP5 models to simulate North Atlantic extratropical cyclones. *J. Climate*, **26**, 5379–5396, https://doi.org/10.1175/JCLI-D-12-00501.1.

Zhang, C., Wang, Y. and Hamilton, Kevin. (2011) Improved representation of boundary layer clouds over the southeast pacific in ARW–WRF using a modified Tiedtke cumulus parameterization scheme. Mon. Wea. Rev., 139, 3489–3513, https://doi.org/10.1175/MWR-D-10-05091.1.

Zhang, D.-L. and Cho, H.-R. (1992) The development of negative moist potential vorticity in the stratiform region of a simulated squall line. *Mon. Wea. Rev.*, **120**, 1322–1341, https://doi.org/10.1175/1520-0493(1992)120<1322:TDONMP>2.0.CO;2.

—— and —— (1995) Three-dimensional simulation of frontal rainbands and conditional symmetric instability in the Eady-wave model, *Tellus A: Dynamic Meteorology and Oceanography*, **47:1**, 45-61, https://doi.org/10.3402/tellusa.v47i1.11493.

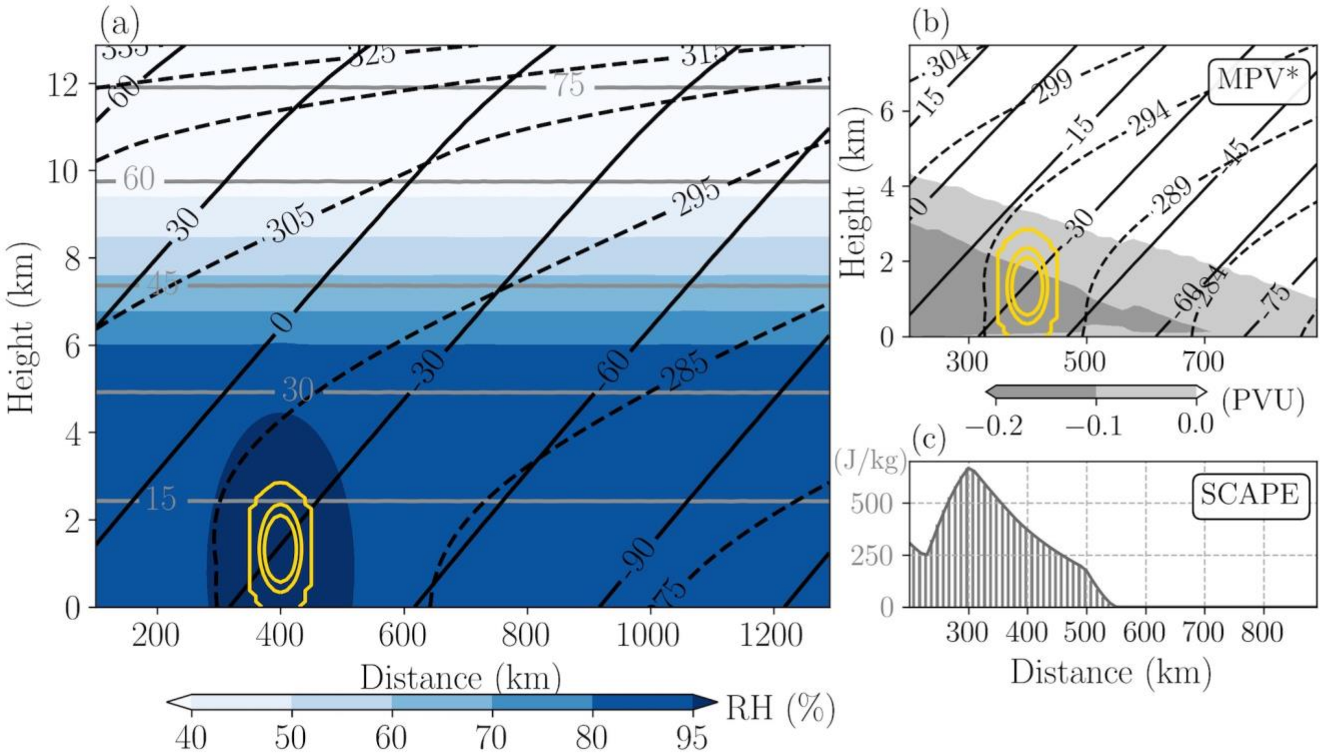

Figure 1. Initial conditions: (a) relative humidity (shading; %), geostrophic wind (gray solid; m s^{-1}), θ_e^* surfaces (black dashed; K), M_g surfaces (black solid; m s^{-1}) and (b) saturation equivalent geostrophic potential vorticity, MPV_g^* (shading; PVU; see (1)). The yellow contours of 0, 0.2, and 0.4 K indicate the initial potential temperature perturbation. (c) Shows the initial SCAPE (bar; J kg^{-1}; see (2)) at the location where the corresponding M_g surface intersects the ground.

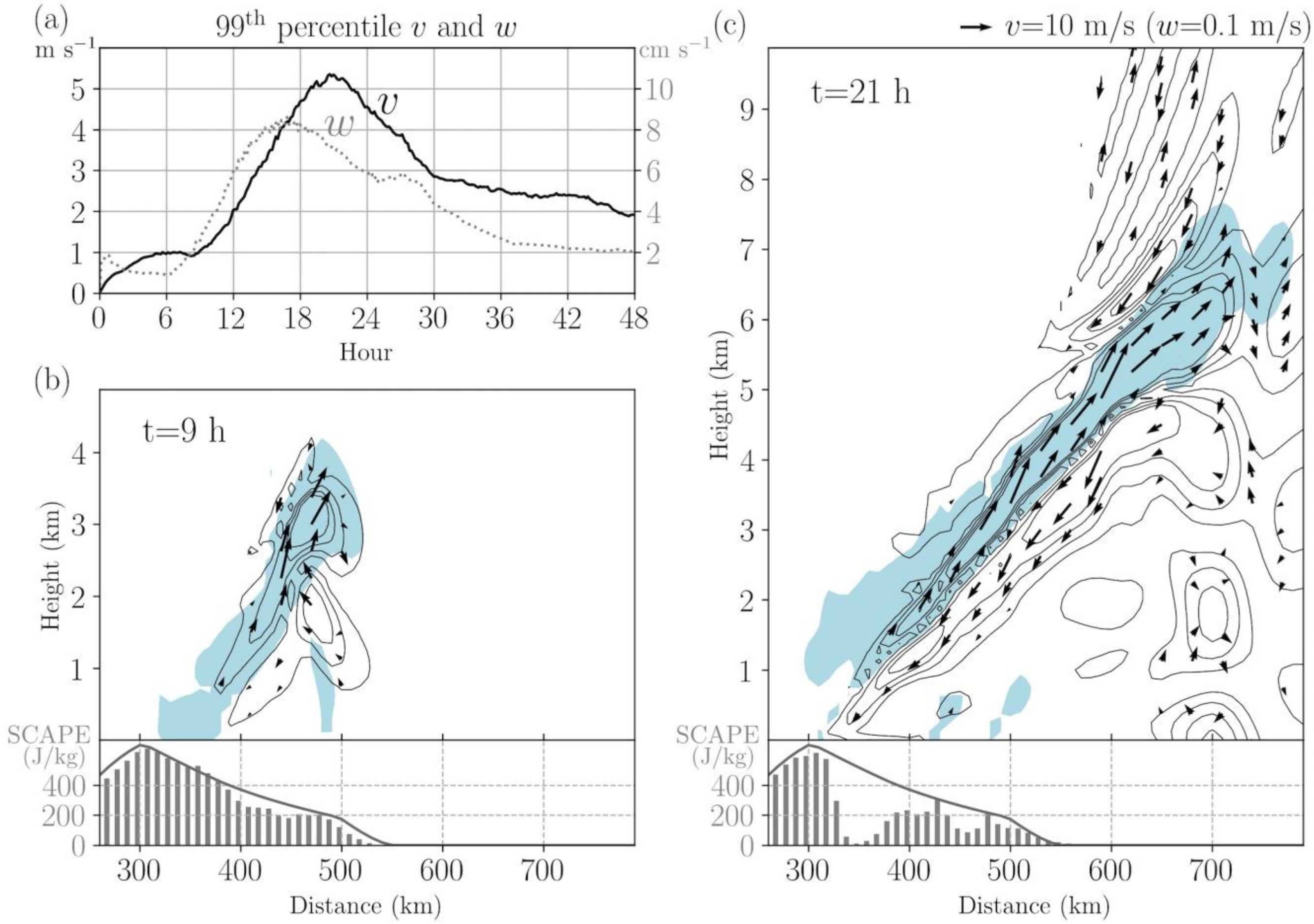

Figure 2. Results for $\Delta y = 10$ km. (a) The time evolution of the 99th percentile v (black; m s^{-1}) and w (gray; cm s^{-1}) over the entire domain. (b) The slantwise transverse circulation (v, w) (vectors), wind speed (contours starting from 0 m s^{-1} with an interval of 1 m s^{-1}), RH≥100 % (light blue shading) at 9 h. The lower panel shows the SCAPE (gray bar shows the current value while the solid gray line shows the initial value; J kg^{-1}), recorded at the location where the sloped M_g surface intersects the ground. (c) Same as (b) but for 21 h.

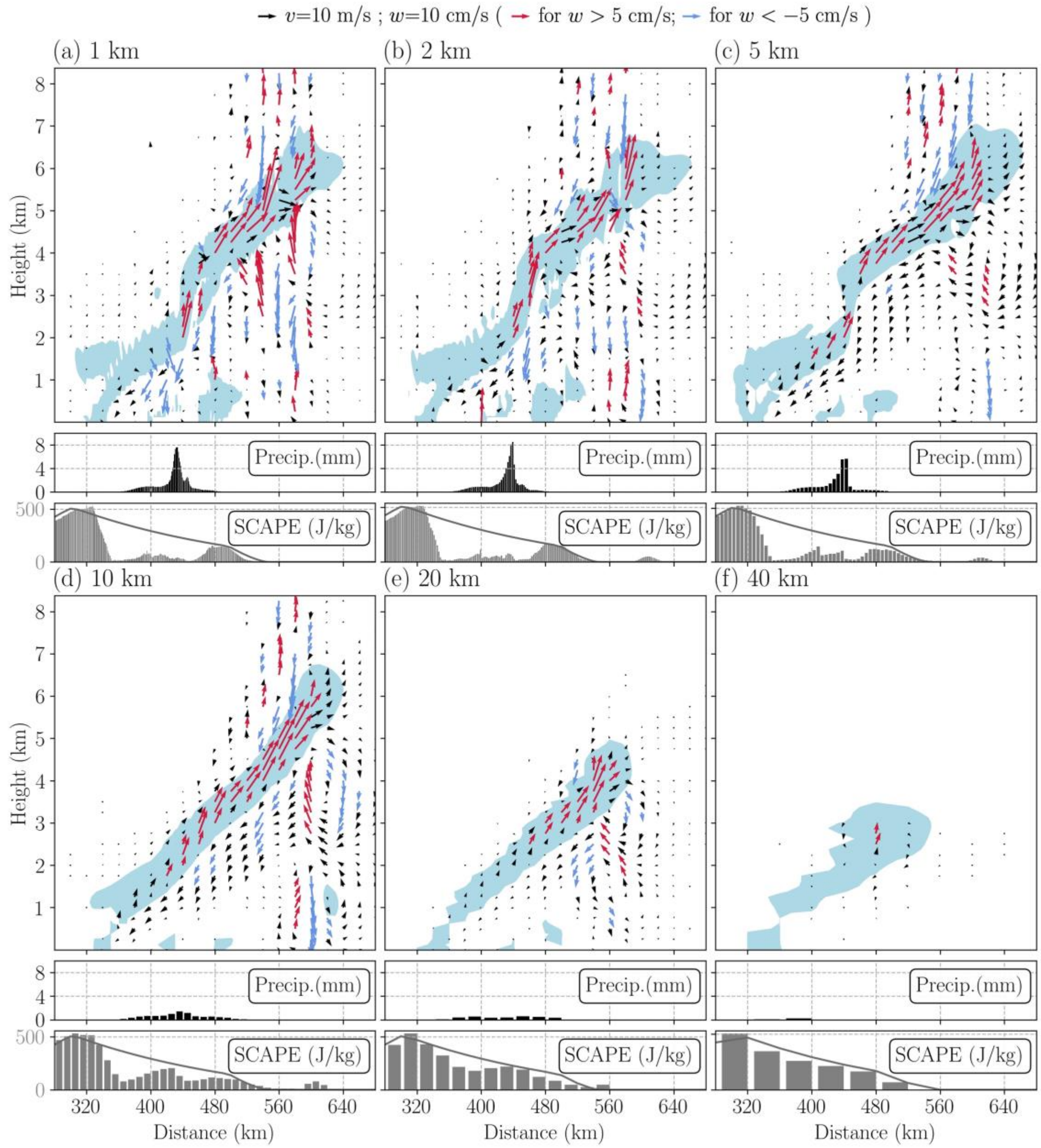

Figure 3. The slantwise convection for Δy of (a) 1 km, (b) 2 km, (c) 5 km, (d) 10 km, (e) 20 km and (f) 40 km at 16 h. The uppermost panel shows areas with RH≥100 % (light blue shading) and the transverse circulation (v, w) (vectors; strong ascent with $w > 5$ cm s^{-1} and decent with $w < -5$ cm s^{-1} are marked in red and blue, respectively). The lower two panels show the accumulated precipitation (black bars; mm) and SCAPE (gray bars; J kg^{-1}), respectively, and the latter is shown at the location where the M_{g} intersects the ground.

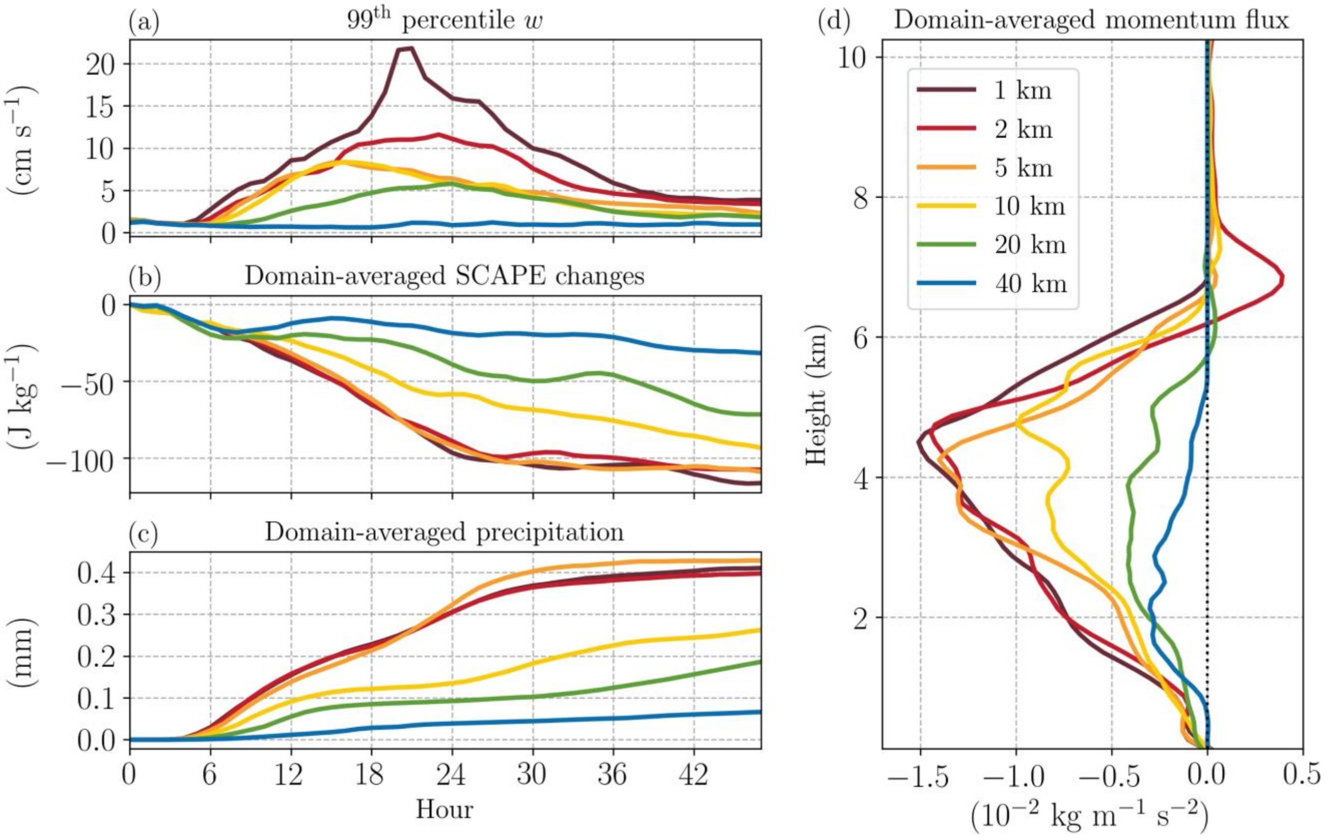

Figure 4. The time evolution of the (a) 99th percentile vertical velocity of the domain, (b) domain-averaged SCAPE difference from the initial time and (c) domain-averaged precipitation. (d) 48-hour- and domain-averaged zonal momentum flux for experiments with different horizontal grid spacings as indicated in the legend. The area used for these calculations is bounded by y =200 and 1000 km.

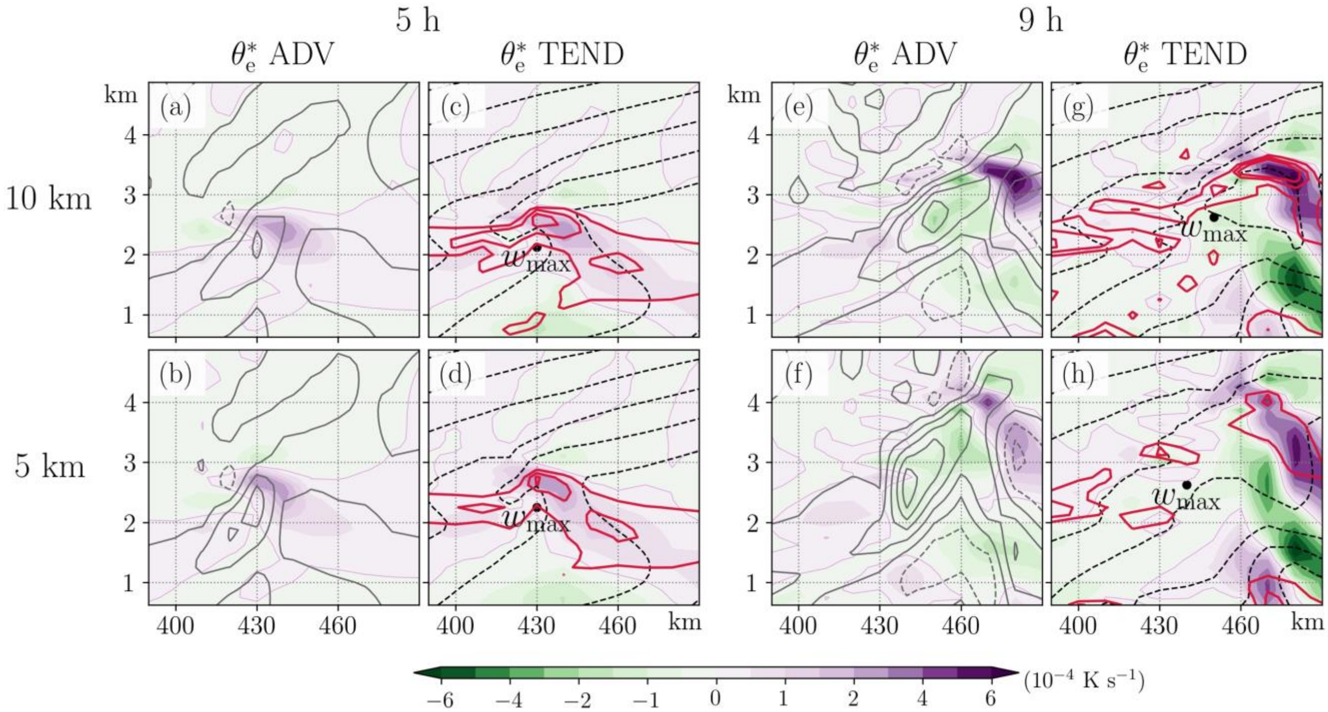

Figure 5. The estimated θ_e^* advection (shading) and w (gray solid and dashed lines indicate the positive and negative values with an interval of 5 cm s^{-1}, respectively) for (a) Δy=10 km and (b) Δy=5 km at 5 h. The concurrent local θ_e^* tendency (shading), θ_e^* (black dashed contours) and the conditional instability, i.e., $\frac{\partial \theta_e^*}{\partial z} < 0$, (red contours with an interval of $-1\text{x}10^{-3}$ K m^{-1}) are shown in (c) for Δy=10 km and in (d) forΔy=5 km. The location of maximum w is also noted. (e)-(h) are the same as (a)-(d), respectively, but at 9 h. For $\Delta y = 5$ km, all fields are averaged onto the same 10-km grid to smooth out the smaller-scale noise.

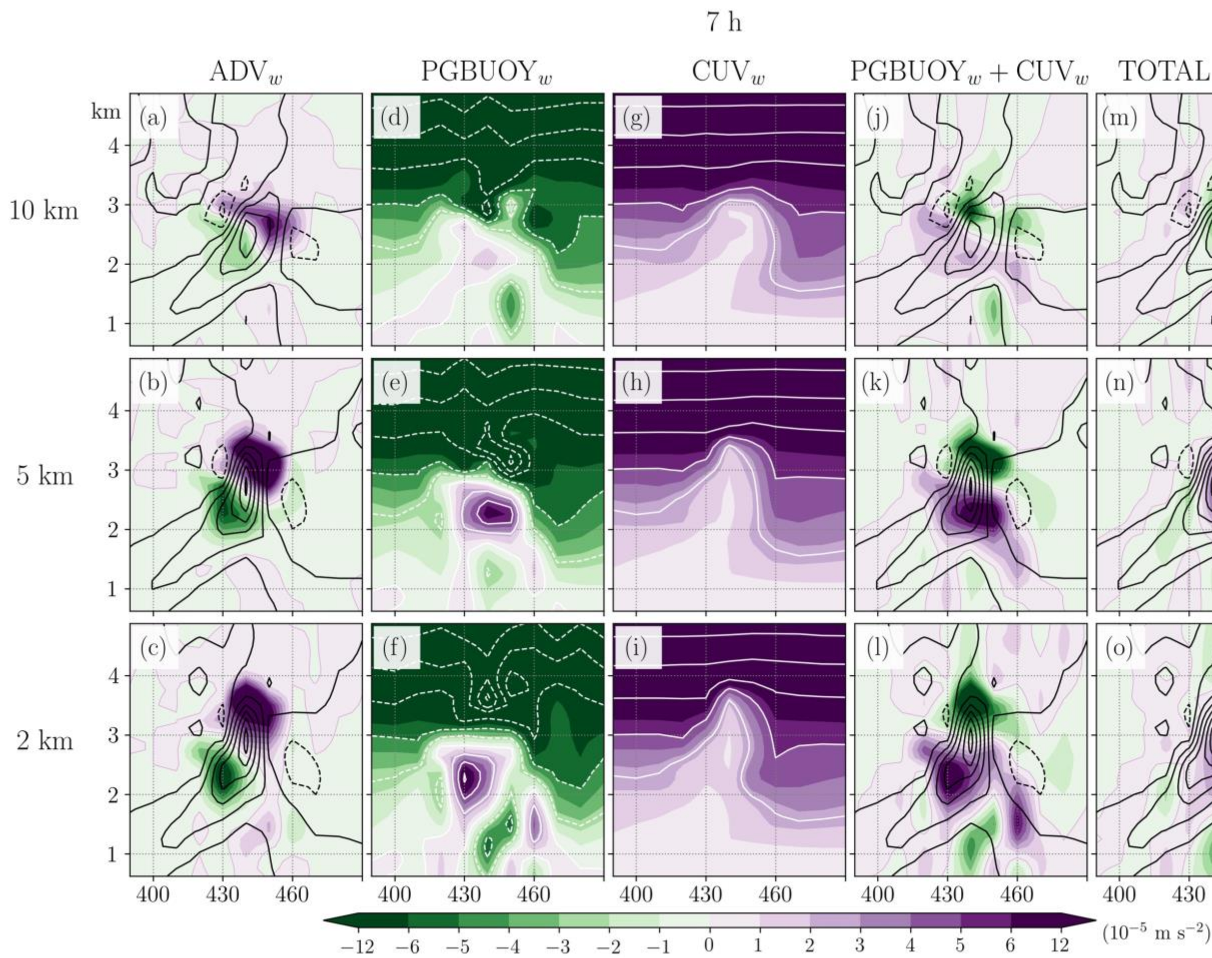

Figure 6. Inline budget analysis of w at 7 h. Each shaded panel from left to right shows the (a)-(c) advection (ADV_w), (d)-(f) net vertical pressure gradient and buoyancy force (PGBUOY_w), (g)-(i) curvature (CUV_w) (solid and dashed white contours indicate positive and negative values, respectively, with an interval of 2.5×10^{-5} m s^{-2}), (j)-(l) the net force of PGBUOY_w and CUV_w [(5); the damping term is small and thus not shown] and (m)-(o) the total tendency. All terms have a uniform unit of m s^{-2}. The top, mid- and bottom rows are for runs with Δy=10, 5 and 2 km, respectively. The black contours indicate w with an interval of 5 cm s^{-1} (positive and negative values shown in solid and dashed lines, respectively). For $\Delta y \leq 5$ km, all fields are averaged onto the same 10-km grid.

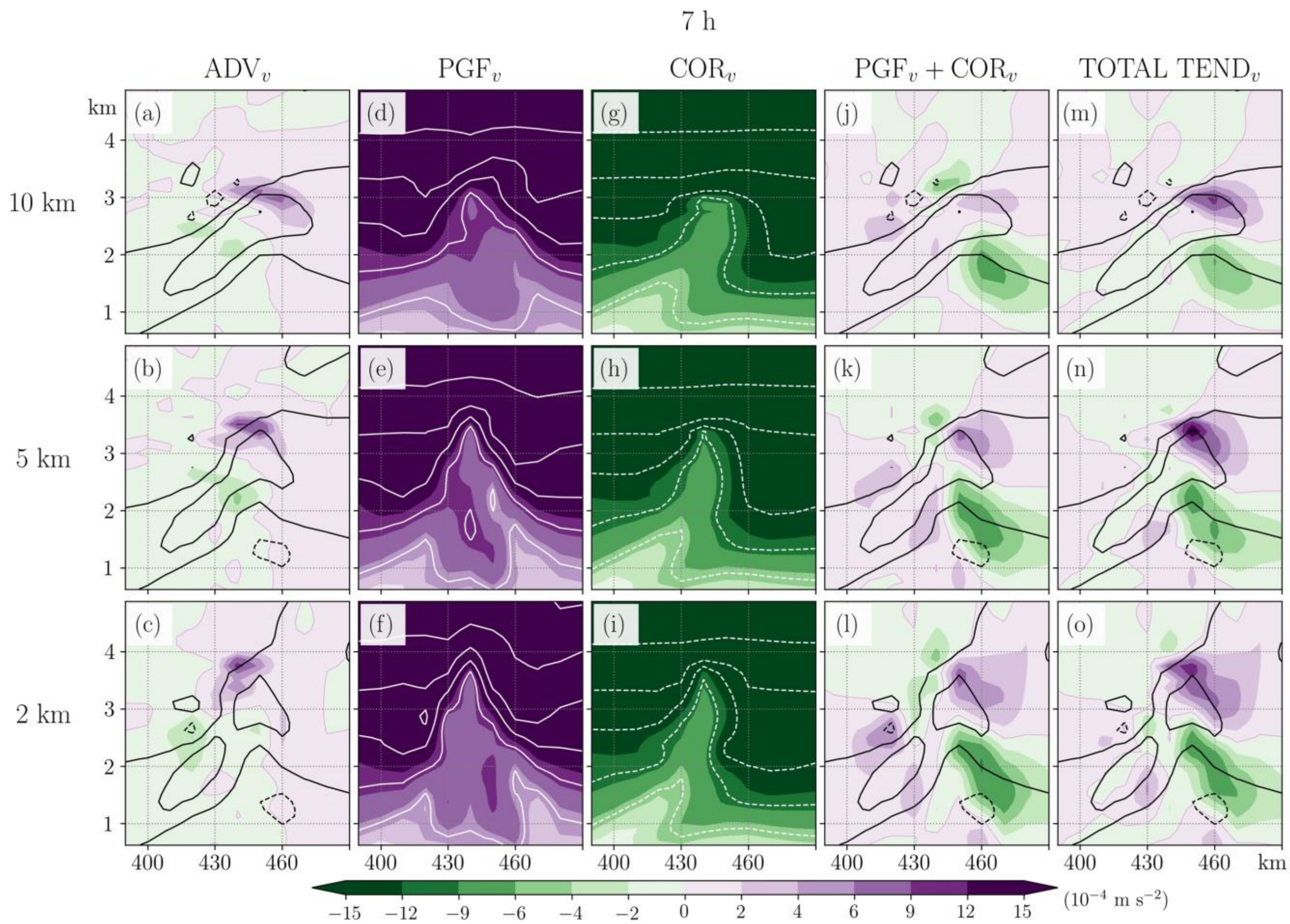

Figure 7. Inline budget analysis of v at 7 h. Each shaded panel from left to right shows the (a)-(c) advection (ADV$_v$), (d)-(f) horizontal pressure gradient force (PGF_v), (g)-(i) Coriolis force (COR_v) (solid and dashed white contours indicate positive and negative values, respectively, with an interval of 5×10^{-4} m s^{-2}), (j)-(l) the net force of PGF_v and COR_v [(4); the curvature term (CUV_v) is small and thus not shown] and (m)-(o) the total tendency. All terms have a uniform unit of m s^{-2}. The top, mid- and bottom rows are for runs with Δy=10, 5 and 2 km, respectively. The black contours indicate v with an interval of 2 m s^{-1} (positive and negative values shown in solid and dashed lines, respectively). For $\Delta y \leq 5$ km, all fields are averaged onto the same 10-km grid.

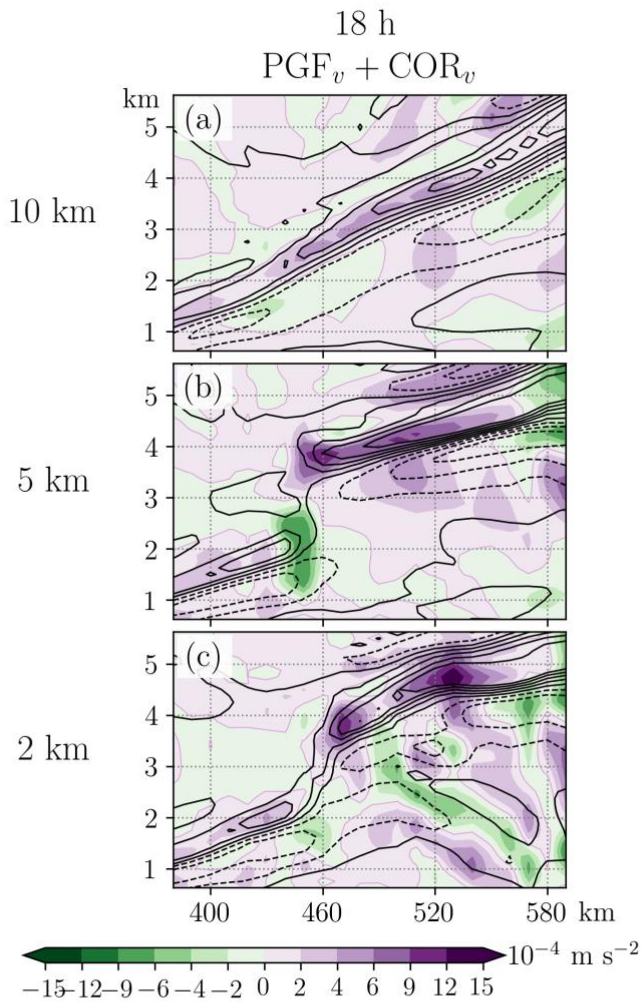

Figure 8. The net force of PGF_v and COR_v (shading) for $\Delta y =$ (a) 10 km, (b) 5, and (c) 2 km runs at 18 h. The black contours indicate v with an interval of 2 m s^{-1} (solid for positive and dashed for negative values). For $\Delta y \leq 5$ km, all fields are averaged onto the same 10-km grid.

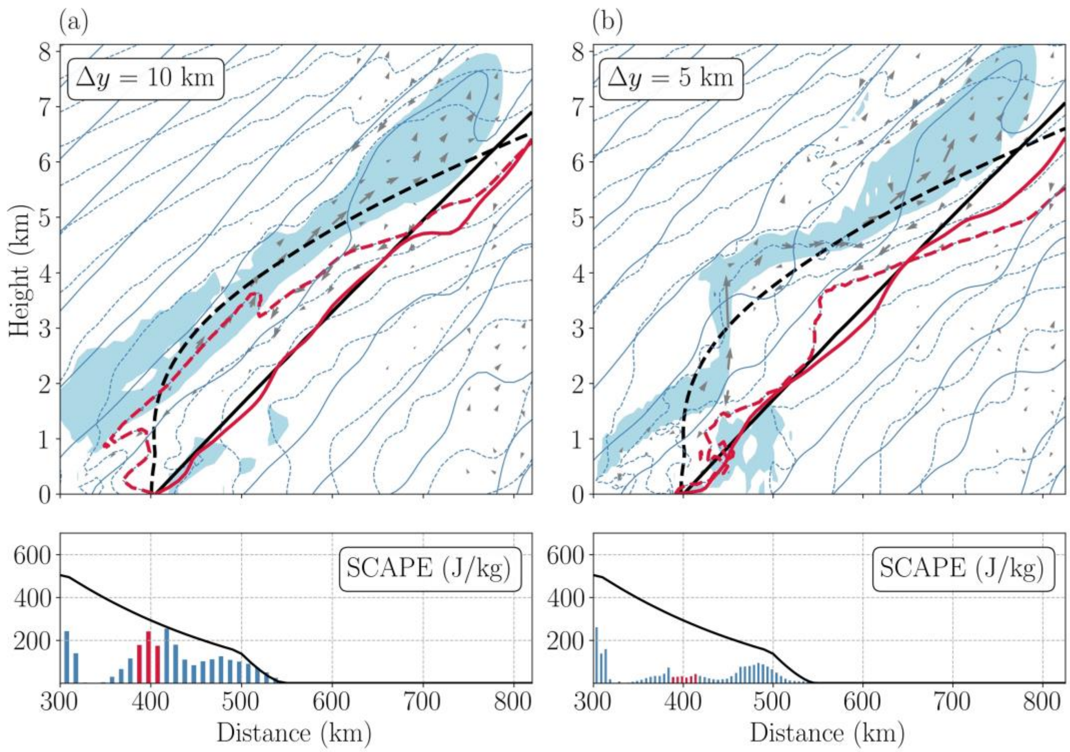

Figure 9. Conditions after the CSI adjustment at 24 h for $\Delta y =$ (a) 10 km, (b) 5 km. The upper panel shows the transverse circulation (v, w) (gray vectors), the M_{g} (solid blue) and θ_{e}^{*} surfaces (dashed blue), RH≥100 % (light blue shading). The lower panel shows the SCAPE (blue bar; J kg^{-1}) at the location where the M_{g} intersects the ground. The black solid line in the lower panel shows the initial SCAPE values. Some example of SCAPE calculation for hypothetical air tubes lifted from near the surface at y ~ 400 km are marked in red. Thick solid and dashed lines in the upper panel indicate the corresponding M_{g} and θ_{e}^{*} surfaces at the initial time (black) and 24 h (red), respectively.

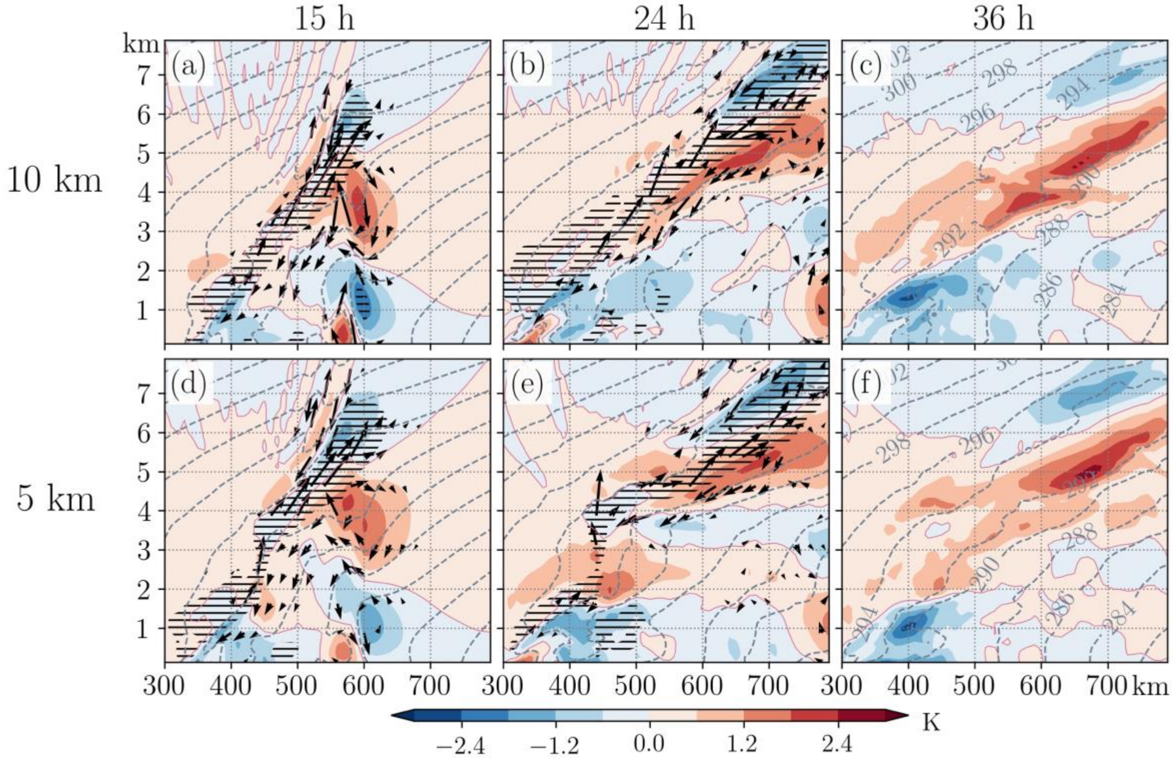

Figure 10. The θ_e^* (dashed contours) and the θ_e^* deviation from its initial field (shading) at (a) 15 h, (b) 24 h and (c) 36 h for Δy =10 km. For earlier times (a) and (b), the transverse circulation (v, w) is also shown (vectors). Areas with RH≥100 % are hatched with horizontal black lines. (d)-(f) are the same as (a)-(c) but for Δy =5, whose fields shown here are averaged onto the same 10-km grid.